ADVANCED MATERIALS
www.advmat.de

Superior Adhesion of Monolayer Amorphous Carbon to Copper

Hongji Zhang, Artem K. Grebenko, Konstantin V. Iakoubovskii, Hanning Zhang, Ruslan Yamaletdinov, Anna Makarova, Alexander Fedorov, Rejaul SK, Ranjith Shivajirao, Zheng Jue Tong, Sergey Grebenchuk, Ugur Karadeniz, Lu Shi, Denis V. Vyalikh, Ya He, Andrei Starkov, Alena A. Alekseeva, Chuan Chu Tee, Carlo Mendoza Orofeo, Junhao Lin, Kazutomo Suenaga, Michel Bosman, Maciej Koperski, Bent Weber, Kostya S. Novoselov, Oleg V. Yazyev, Chee-Tat Toh, and Barbaros Özyilmaz**

The single-atom thickness of graphene holds great potential for device scaling, but its effectiveness as a thin metal-ion diffusion barrier in microelectronics and a corrosion barrier for plasmonic devices is compromised by weak van der Waals interactions with copper (Cu), leading to delamination issues. In contrast, monolayer amorphous carbon (MAC), a recently reported single-atom-thick carbon film with a disordered sp^2 hybridized structure, demonstrates superior adhesion properties. This study reveals that MAC exhibits an adhesion energy of 85 J m^{-2} on Cu, which is 13 times greater than that of graphene. This exceptional adhesion is attributed to the formation of covalent-like Cu—C bonds while preserving its sp^2 structure, as evidenced by X-ray photoelectron spectroscopy (XPS) and near-edge X-ray absorption fine structure (NEXAFS) spectroscopy. Density functional theory (DFT) calculations further elucidate that the corrugated structure of MAC facilitates the hybridization of C $2p_z$ orbitals with Cu 4s and $3dz^2$ orbitals, promoting strong bonding. These insights indicate that the amorphous structure of MAC significantly enhances adhesion while preserving its elemental composition, providing a pathway to improve the mechanical reliability and performance of two-dimensional (2D) materials on metal substrates in various technological applications.

1. Introduction

Copper (Cu) is widely used in various applications due to its excellent thermal and electrical conductivity. Its relatively low chemical reactivity, compared to metals like iron, is largely attributed to the formation of a protective Cu oxide layer that inhibits further corrosion.[1] However, when employed in microelectronic devices, Cu requires additional protective barriers to prevent metal ion diffusion and corrosion.[2,3] As these devices continue to scale down, it is crucial to develop thinner barrier films to meet the demands of miniaturization.

To address these challenges, 2D materials, particularly graphene, have been extensively studied as ultrathin barrier films for Cu.[2,3] Graphene is favoured not only because it can be directly grown on Cu[4] but also due to its exceptional properties, including high mechanical strength, impermeability, thermal stability,

H. Zhang, A. K. Grebenko, K. V. Iakoubovskii, A. A. Alekseeva, C.-T. Toh, B. Özyilmaz
Department of Physics
National University of Singapore
Singapore 117551, Singapore
E-mail: chee_tat@nus.edu.sg; barbaros@nus.edu.sg

H. Zhang, U. Karadeniz, L. Shi, Y. He, A. Starkov, C. C. Tee, C. M. Orofeo, M. Bosman, M. Koperski, C.-T. Toh, B. Özyilmaz
Department of Materials Science and Engineering
National University of Singapore
Singapore 117575, Singapore

The ORCID identification number(s) for the author(s) of this article can be found under https://doi.org/10.1002/adma.202419112

DOI: 10.1002/adma.202419112

H. Zhang, R. Yamaletdinov, O. V. Yazyev
Institute of Physics
Ecole Polytechnique Fédérale de Lausanne (EPFL)
Lausanne CH-1015, Switzerland

A. Makarova, A. Fedorov
Helmholtz-Zentrum Berlin für Materialien und Energie
14109 Berlin, Germany

A. Fedorov
Leibniz Institute for Solid State and Materials Research
01069 Dresden, Germany

A. Fedorov
Joint Laboratory "Functional Quantum Materials" at BESSY II
12489 Berlin, Germany

R. SK, R. Shivajirao, Z. J. Tong, B. Weber
Division of Physics and Applied Physics
School of Physical and Mathematical Sciences
Nanyang Technological University
Singapore 637371, Singapore

chemical inertness, and the ability to maintain its structural integrity at a single-atom thickness.[5] Graphene has shown promising results as a corrosion barrier for plasmonic devices, and as a passivation and Cu diffusion-blocking layer in metal interconnects and solar cells.[2,6,7] However, a major challenge in these applications is the tendency of graphene to delaminate from Cu surfaces, primarily due to weak van der Waals interactions.[8–11] Various strategies have been explored to enhance the adhesion between graphene and Cu, such as alloying Cu with other metals,[9,10] functionalising graphene with chemical groups,[11] and introducing defects into graphene.[12] Despite these efforts, such methods often have drawbacks, including altering the intrinsic properties of Cu, increasing the barrier thickness, or compromising the barrier properties of graphene.

The recent discovery of monolayer amorphous carbon (MAC) offers a novel approach to addressing these issues.[13] Unlike its crystalline counterpart, MAC provides a balanced solution for graphene applications. It exhibits a Young's modulus of 200 GPa, comparable to chemical vapor deposition (CVD) graphene, but with seven times higher fracture toughness, and can be directly grown on pre-patterned structures at low temperature (250 °C).[14] Furthermore, MAC maintains excellent ion impermeability and possesses a sub-nanometre thickness.[15]

In this study, we investigated the adhesion properties of MAC synthesized by laser-assisted CVD on Cu foils. Remarkably, we measured an adhesion energy of 85 J m^{-2}, which is 13 times higher than that of graphene on Cu. This value significantly exceeds the threshold adhesion values required during processes like chemical mechanical polishing,[16] allowing for increased mechanical reliability. Our analysis suggests that electrostatic and van der Waals forces do not significantly contribute to this high adhesion. Instead, X-ray photoelectron spectroscopy (XPS) and near-edge X-ray absorption fine structure (NEXAFS) spectroscopy investigations indicate the formation of covalent-like Cu—C bonds between a fraction of carbon atoms in MAC and the surface Cu atoms. Density functional theory (DFT) modelling proposes that the presence of topological defects and corrugation in MAC enhances the hybridization of carbon $2p_z$ orbitals with Cu 4s and $3dz^2$ orbitals. This hybridization effect is weak in graphene but becomes possible in MAC due to its unique structure, which enables hybridization of C with Cu while preserving the MAC sp^2 amorphous atomic arrangement.

2. Results and Discussion

2.1. Basic Characterization of the MAC Grown on Cu

MAC exhibits significant structural corrugation due to its amorphous structure, as schematically illustrated in **Figure 1a**. This atomic-scale corrugation arises from the disordered arrangement of carbon atoms forming 5-, 6-, 7-, and 8-member rings, predominantly with three-fold coordination, as observed in freestanding MAC using aberration-corrected transmission electron microscopy (TEM) (Figure 1b).[15] In a typical MAC sample, the ratio of hexagonal to non-hexagonal rings is ≈6:4, with most hexagonal rings exhibiting significant out-of-plane strain and deformation. This corrugation is supported by cross-sectional TEM measurements of as-grown MAC layer on metal substrate (Figure 1c; Figure S1, Supporting Information) and scanning tunnelling microscopy (STM) of MAC film transferred to flash-annealed gold on Mica substrate (Figure 1d).

The constant-current scanning tunnelling microscopy (STM) topography reveals the absence of long-range order, confirming the amorphous nature of MAC. The presence of non-hexagonal rings interspersed with hexagonal motifs leads to a complex defect network, which induces significant variations in the local density of states (LDOS). These inhomogeneities in electronic structure, coupled with the lack of periodicity, pose substantial challenges in resolving the precise atomic configuration. However, the STM topography in Figure 1d clearly exhibits a corrugated surface. The roughness analysis of the topography yields an root mean square (RMS) roughness of ≈4.8 Å on a lateral scale of a few nanometers (Figure 1e). Given that the thickness of an individual carbon atom is ≈2.8 Å, this corresponds to an overall thickness of ≈8 Å, which corroborates our claim of large intrinsic corrugation. Atomic force microscopy (AFM) analysis of the transferred film (Figure 1f) indicates a monolayer thickness of 0.8 nm on the substrate and an interlayer distance of 0.6 nm when stacked, which is notably twice the thickness of graphene.[17]

These structural characteristics are further corroborated by Raman spectroscopy results. Compared to graphene, which also features a fully sp^2 structure, the Raman spectrum of freestanding MAC has a prominent D peak, which indicates disruption of hexagonal symmetry (Figure 1g). The broad full width at half maximum (FWHM) of the D and G peaks suggests a wide distribution of distortions in non-hexagonal carbon rings, reflecting variations in bond lengths and angles.[18] The I_D/I_G ratio of <1 suggests that MAC is predominantly amorphous without any localized crystalline, thereby confirming its amorphous structure.[19]

S. Grebenchuk, M. Koperski, K. S. Novoselov, B. Özyilmaz
Institute for Functional Intelligent Materials
National University of Singapore
Singapore 117544, Singapore
D. V. Vyalikh
Donostia International Physics Center (DIPC)
Donostia-San Sebastián 20018, Spain
D. V. Vyalikh
IKERBASQUE Basque Foundation for Science
Bilbao E-48009, Spain
J. Lin
Department of Physics
Southern University of Science and Technology
Shenzhen 518055, China
K. Suenaga
Sanken
Osaka University
Ibaraki, Osaka 567-0047, Japan
C.-T. Toh, B. Özyilmaz
Centre for Advanced 2D Material Singapore
National University of Singapore
Singapore 117546, Singapore

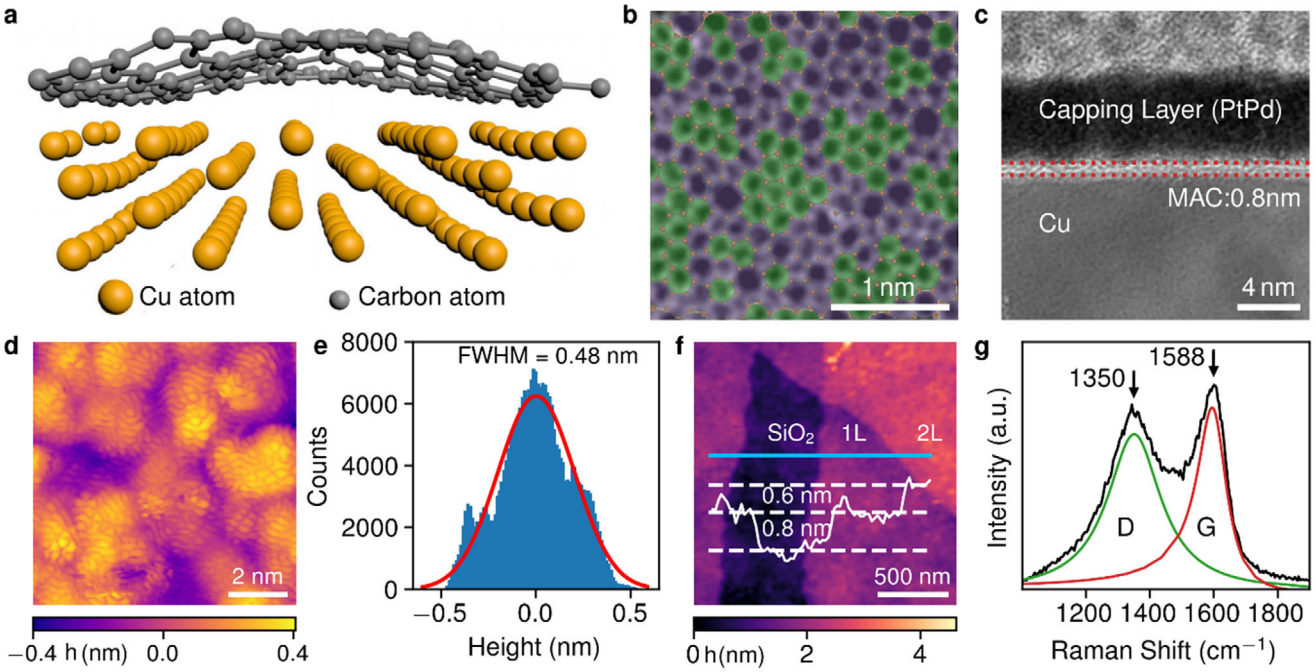

Figure 1. Characterisation of MAC structure. a) Schematic of the atomic corrugation of MAC on Cu. b) TEM image of MAC with false colour overlay added for identification of regular hexagonal rings (green), and non-hexagonal or distorted hexagonal rings (purple). c) Cross-sectional TEM image at the PtPd-MAC-Cu interface with a uniform MAC thickness of 0.8 nm. d) Atomic-resolution STM topography of the MAC layer at Vbias = 300 mV, and I_T = 300pA. e) Height distribution histogram obtained from topography in d showing RMS roughness of 0.48 nm. f) AFM image of 1 and 2 layers of MAC on SiO_2/Si. The blue line indicates the line-scan position for the overlaid height profile. g) Raman spectrum of free-standing MAC measured with 532 nm excitation wavelength.

2.2. Direct Measurement of Interface Adhesion

There are several established tests for measuring adhesion energy, including the double cantilever beam (DCB), blister, indentation, and peeling tests.[20,21] One way to differentiate these techniques is by their loading mode.[22] In fracture mechanics, the primary loading modes are recognized as opening (Mode I), shearing (Mode II), and tearing (Mode III). Double cantilever beam (DCB) tests, operating under pure Mode I, and blister tests, which combine Mode I and Mode II loading, have long been used to measure adhesion energy in 2D systems.

Regarding the graphene–Cu interface, the first measurements of adhesion energy between evaporated Cu and graphene using the DCB method—as reported by Yoon et al.—yielded a value of 0.72 J m^{-2}.[23] Subsequent DCB tests conducted by Na et al. on graphene on Cu foil indicated higher adhesion energies of 6.0 J m^{-2} (for the graphene–Cu interface).[24] The difference was later shown by the author to be due to the difference in roughness of the underlying substrate and not due to differences in energy dissipation in the two methods.[23,24]

Recently, the peeling test—also involving both Mode I and Mode II—has emerged as an attractive, simple, and practically important alternative. Advances in the theoretical framework that incorporate the consideration of dissipation energy now enable the extraction of intrinsic interface fracture toughness (i.e., adhesion energy) from peeling tests, yielding values comparable to those derived from Mode I Linear Elastic Fracture Mechanics tests, such as the DCB.[22,25–27]

In our research, interface adhesion energy between MAC/Cu foil and graphene/Cu foil was directly measured using a conventional 90° peeling test (**Figure 2a**).[25] The Cu substrate functioned as a thin, relatively rigid peeling arm. Ethyl cyanoacrylate (ECA) was used as the standard adhesive due to its strong adhesion properties and was reported to be suitable for carbon thin films.[28,29] After drying, ECA formed a rigid layer that can help to minimize the influence of stick-slip effects.[30,31] Overall, the careful selection of adhesive and peeling arm properties minimizes additional dissipation energy components (see Note S1, Supporting Information), allowing our measurements to be directly compared with previous studies on graphene deposited on Cu foil. The solubility of ECA in acetone further facilitates analysis of the transferred carbon films. Notable, for CVD graphene on Cu foil we measured an adhesion energy of 6.5 J m^{-2} (Figure 2b), which closely aligns with the 6.0 J m^{-2} value reported for the Cu foil/graphene interface in earlier DCB tests conducted under similar conditions, including comparable Cu foil roughness and adhesive rigidity.[24]

In our investigation of MAC samples, we measured an adhesion energy of 85 ± 4.2 J m^{-2} (Figure 2b; Figure S2a, Supporting Information), which is ≈13 times greater than that of graphene. A detailed analysis of the fracture energy and potential energy dissipation indicates that the measured adhesion energy of MAC to Cu may overestimate the intrinsic adhesion energy by no more than 10% (Note S1, Supporting Information). Nevertheless, to remain cautious, we emphasize that our observation reports the relative enhancement of the adhesion energy within the same type

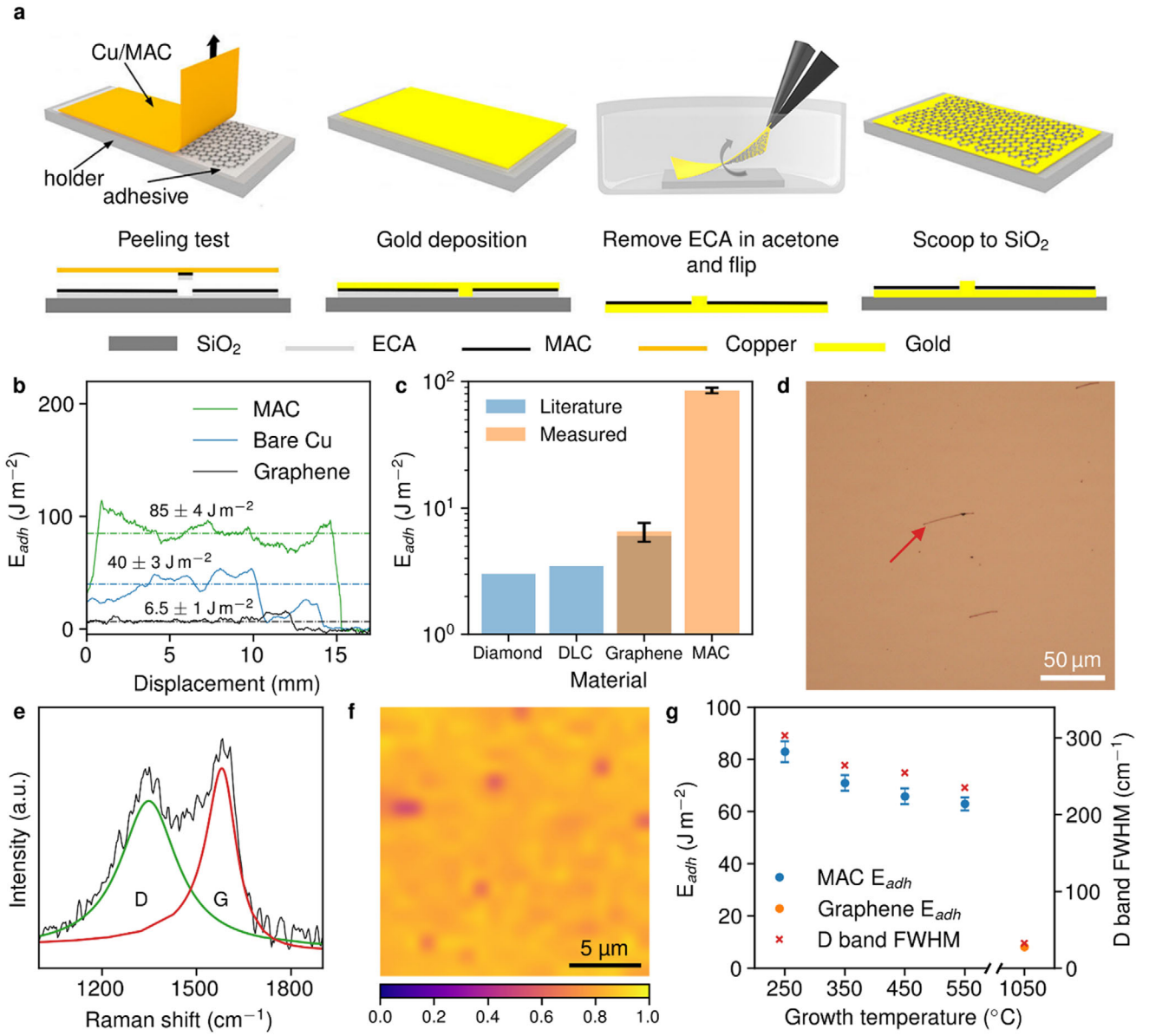

Figure 2. Direct measurements of Cu-MAC adhesion. a) Schematics of the 90° peeling test and subsequent transfer of the peeled MAC layer from the adhesive to SiO_2/Si wafer using a gold support layer. b) Measured adhesion energy for MAC to Cu, bare Cu to ECA, and graphene on Cu. c) Comparison of the adhesion energy between Cu and various forms of thin-film carbon. d) Optical image of peeled-off MAC on Au on SiO_2/Si wafer. A uniform surface with a few line patterns (indicated by the red arrow) is seen. e) Raman spectrum of MAC under 532 nm excitation. f) Raman map showing the I_D/I_G intensity ratio of MAC in (e). g) Growth temperature dependence of the adhesion energy of MAC or graphene to Cu (dots) and their D band full width at half maximum (FWHM) (red crosses).

of test for MAC and graphene on the same type of Cu. We further corroborated this enhancement through a pure Mode II test using a shear force test configuration. Here we observe a 10-fold increase in fracture energy for the MAC/Cu interface compared to graphene/Cu (see Figure S2b,c, Supporting Information). Besides graphene, the adhesion energy between MAC and Cu is also much higher compared to the adhesion energy between other carbon-only materials and Cu, including diamond-like carbon (DLC) and diamond, which are both reported to be ≈3 J m^{-2}.[32–34]

The completeness of as-grown MAC film on Cu is confirmed by both oxidation test and Raman mapping, as shown in Figures S3 and S4 (Supporting Information). To ensure the completeness of the MAC after peeling, it is necessary to isolate it from ECA for further characterization. This process involves depositing a gold support layer on the MAC adhered to ECA, followed by dissolving the ECA in acetone (Figure 2a). The MAC, now supported by gold, is being flipped in acetone by a tweezer and then transferred onto a SiO_2/Si substrate. The optical image of the transferred MAC on Au (Figure 2d) has a generally uniform surface with a few line patterns. Further analysis using AFM revealed that these lines are protrusions corresponding to cracks formed in ECA during the peeling test (Figure S5a, Supporting

Information). Similar features are also observed in graphene (Figure S5b, Supporting Information), indicating that these features do not significantly affect the measured maximum adhesion energy, ensuring that the adhesion values accurately reflect the interaction between MAC and the copper substrate.[30] Raman spectrum of the transferred MAC after peeling gives an I_D/I_G ratio of 0.8 (Figure 2e), indicating there is no structural change during the peeling process. Further spatial map of Raman scattering response of MAC showed consistent intensity of G and D bands with an I_D/I_G ratio of 0.8 (Figure 2f), confirming the integrity of the MAC post-transfer. Although a few spots with lower I_D/I_G ratios appeared in the mapping, they still provided a distinct MAC signal, indicating that these variations might arise from defects caused by the transfer process. Moreover, the continuity of MAC proves that the measured adhesion energy is primarily attributed to the interaction between MAC and the Cu substrate.

We also conducted peeling tests for MAC samples grown at different temperatures (250, 350, 450, and 550 °C) to understand how adhesion energy correlates with the degree of structural disorder (Figure 2g). Analysis of the Raman spectra showed that the full width at half maximum (FWHM) of the D band narrows with increasing growth temperature, indicating reduced disorder in MAC.[18] Consequently, the adhesion between Cu and MAC decreases as the FWHM of the D peak narrows, suggesting that adhesion energy increases as the structure transitions from crystalline graphene to substantially disordered MAC.

2.3. Microscopic Analysis of the Mechanism Behind Strong Adhesion

For the case of the adhesion of graphene to Cu, charge transfer at the interface and the associated electrostatic energy are often considered primary contributions to adhesion.[35–37] Theoretical studies have calculated that the adhesion between two materials is directly proportional to the square of their work function difference.[38] Thus, to estimate this contribution for Cu-MAC, we investigated the work function using Kelvin probe force microscopy (KPFM) illustrated in **Figure 3a**. We used free-standing CVD graphene, transferred from Cu foil to TEM grid with a polymethyl methacrylate (PMMA)-assisted transfer technique, to calibrate the AFM tip, referencing a work function value of 4.3 eV for pristine graphene (Figure S6, Supporting Information).[39] This calibration allowed us to measure relative work function changes in both free-standing and as-grown MAC (on Cu) samples. The surface topography of suspended MAC is free from contamination (Figure 3b) and has an averaged work function of 4.61 ± 0.02 eV (Figure 3c), while MAC on Cu has a work function of 4.56 ± 0.01 eV. Typically, Cu has a work function of 4.5 eV, and the electrostatic interaction between Cu and carbon film is proportional to the square of the work function difference.[40] This is illustrated in Figure 3f, where the change in potential when MAC is on a Cu surface is 0.05 eV, which is smaller than that of graphene at 0.12 eV (Figure S6, Supporting Information). This suggests that the strong adhesion of MAC on Cu originates from factors beyond simple electrostatic interaction due to charge transfer.

To further explore the origin of the exceptionally high adhesion energy values, we examine the MAC-Cu interface and the transferred MAC on SiO_2/Si substrate using XPS and NEXAFS spectroscopy. The XPS C 1*s* line of the MAC-Cu interface suggests the presence of at least three peaks (Figure 3g). The main peak at 284.4 eV is attributed to the sp^2 carbon ring structure, and the peak at higher binding energy corresponds to C—O bonds, which originate from the CO group adsorbed on Cu.[13] Most crucial is the observation of a pronounced peak at 283.8 eV, typically indicative of metal-carbon bonding. However, such a peak was previously not observed in graphene or DLC on Cu. Moreover, this peak is absent in MAC after transferring to a SiO_2/Si substrate, confirming its origin from the interaction with the Cu substrate (Figure S7, Supporting Information).

NEXAFS spectroscopy with polarized X-rays shows strong incidence angle dependence of the 1s-π^* and 1s-σ^* transitions for sp^2 hybridized graphene, where contributions from σ bonds dominate at 90° angle and contributions from π bonds dominate at near-zero angles.[41] For MAC, although polarization dependence is observed, it is less pronounced (Figure S7, Supporting Information). We focus on the 30° angle, where the 1s-π^* transition shows the highest intensity. The contribution of carbon σ bonds to the Cu-MAC interaction is negligible due to their smaller size, while the 1s-σ^* transition line is broad and largely insensitive to incidence angle changes.

Further, we compared the C-K edge NEXAFS spectrum of as-grown MAC on Cu foil with that of MAC transferred to a SiO_2/Si substrate (see Figure 3h). The transfer process naturally leads to the broadening of both the 1s-π^* and 1s-σ^* features, as well as the emergence of additional components between them.[42] A closer inspection of the 1s-π^* resonance region in the as-grown MAC on Cu reveals the presence of at least two components, a similar observation that can be made for the transferred MAC sample as well. Given the wide variety of bonding geometries and coordination numbers in the first three neighboring spheres of individual carbon atoms in MAC, the aforementioned components cannot be directly attributed to specific bonds of carbon atoms. Therefore, we analyze and compare the spectral patterns of the 1s-π* features only in a qualitative manner. While the 1s-π* peak appears noticeably broader after the transfer (blue curve vs red in the inset of Figure 3h), it shifts toward lower photon energies. This indicates stronger interaction between MAC and Cu compared to the MAC on SiO_2/Si substrate. These observations are also in accordance with the earlier reports of graphene adhesion to metallic surfaces. Indeed, the 1s-π* peak position shift toward higher photon energies indicates stronger bonding.[43,44]

2.4. DFT Simulations of the MAC-Cu Interface

To elucidate the origins of the enhanced adhesion strength at the MAC-Cu interface, we performed DFT computations. We constructed a sufficiently large (>100 carbon atoms) model of MAC, using the quench-from-the-melt method[45] and placed it on a five-layer Cu(311) slab (Figure S8, Supporting Information). The relaxed structure as predicted by the dispersion-corrected DFT calculations (**Figure 4a**), reveals a notably broad distribution of carbon atom-to-closest Cu neighbour distances from 2.15 to 4.38 Å (Figure 4b), attributed to the natural buckling of the MAC sheet that persists upon adsorption onto the Cu surface. A comparison with the C-Cu distances from calculated graphene-Cu interfaces (Figure S9, Supporting Information) further enables us to

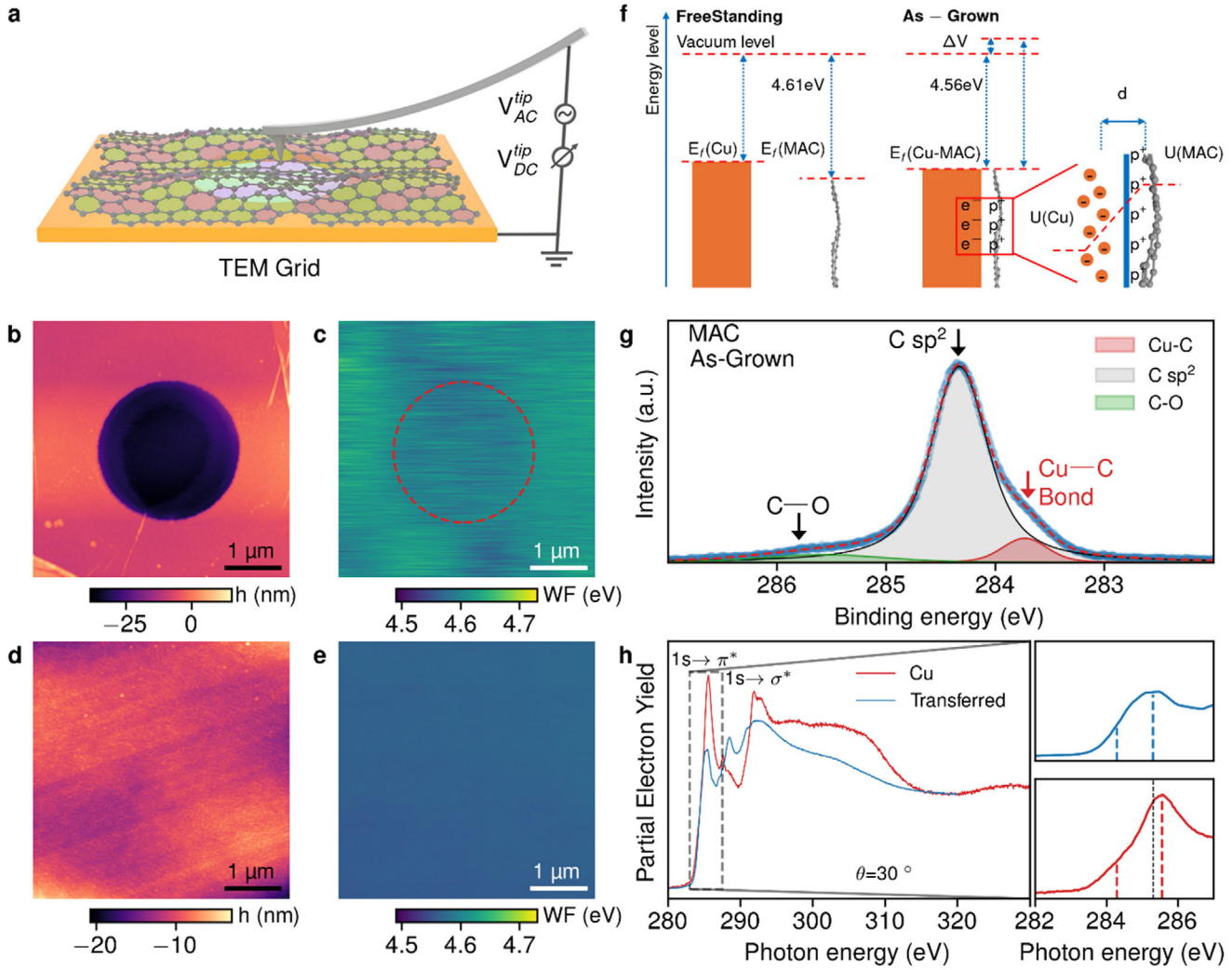

Figure 3. Microscopic analysis of the mechanism behind strong adhesion. a) Schematics of the KPFM measurement of MAC. b) topography and c) work function distribution maps of the free-standing MAC samples. The tip was calibrated over single-layer graphene. d) Topography and e) work function distribution maps of the MAC on Cu foil captured by the same tip. f) Energy diagram depicting the contribution of the charge transfer to overall adhesion. g) High-resolution XPS spectra of as-grown MAC on Cu foil, measured at the beamline using 350 eV photon energy and bandwidth of 100 meV. Gray and green peaks correspond to sp^2-hybridized carbon and various contaminations, respectively. The red-filled peak centred at 283.7 eV corresponds to covalent-like bonding, often denoted as metal-carbon bonds. h) NEXAFS spectra of as grown on Cu (red line) and transferred (blue line) MAC layer captured at 30 degrees of incidence angle of linearly polarized X-rays. A close-up of the 1s-π* transition region is shown on the right. Dotted coloured lines indicate the position of the components. Peak is shifted for as-grown sample (relative to the black dotted line), which indicates stronger adhesion of the carbon layer to Cu.

roughly group the MAC-Cu distances into three distinct regimes: typical graphene-Cu separations between 3.0 and 3.8 Å, accounting for ≈50% of carbon atoms in MAC; C-Cu separations greater than 3.8 Å, comprising 10% of the carbon atoms; and shorter separations below 3.0 Å, which represent the remaining 40% of carbon atoms in MAC.

Employing a crystal orbital Hamiltonian projection (COHP) analysis (Note S2, Supporting Information),[46] stronger adhesion of MAC as compared to graphene can subsequently be illustrated based on these three separation regimes. Figure 4c presents the averaged COHP values for band structure energies between −22 and 2 eV relative to the Fermi level. Beginning with the graphene-Cu regime, we observe that its COHP curve closely resembles that for the graphene-Cu interface, both deviating by less than 0.04 eV from zero throughout the entire spectrum, indicating that their C-Cu pair interactions contribute equally minimally to the formation of covalent-like bonds. The high separation regime COHP even remains completely flat at zero, suggesting virtually no C-Cu interaction. The remaining low-separation-regime COHP, however, shows a lesser peak at −20 eV and three large peaks around −7.5, −5, and −2 eV, implying that the participation of these carbon atoms in strong C-Cu covalent-like bonding crucially contributes to the high adhesion of MAC. An orbital-resolved COHP analysis (Figure S10, Supporting Information) was further performed, allowing the assignment of the precise bonding type to each of these peaks. We find that the positive

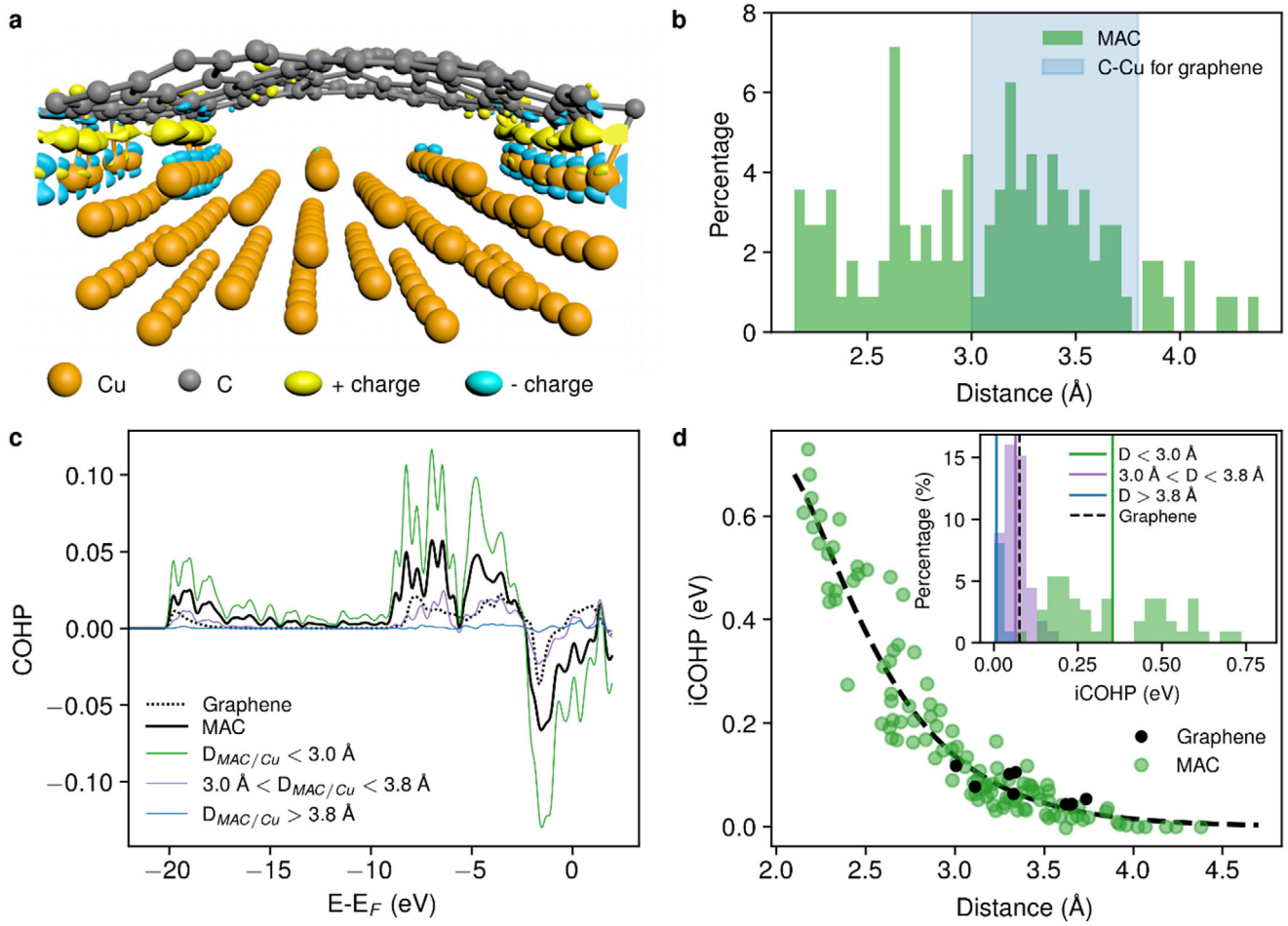

Figure 4. DFT simulations of the Cu-MAC interface. a) Atomic structure of MAC on Cu (311) substrate plotted with the charge density difference at the interface (electron excess in yellow and electron deficiency in blue). b) Distance distribution (from each carbon atom in MAC to the closest Cu atom on the Cu surface). c) Average crystal orbital Hamiltonian projection (COHP) calculated for MAC and graphene between −22 and 2 eV with respect to the Fermi energy. d) Mapping of covalent-like bonding energy to C-Cu distance in both MAC and graphene. The inset shows histograms of the covalent-like binding energy for the three distance regimes and the averages as vertical lines.

peak at −20 eV results from a σ bond between C 2*s* and Cu 4*s* orbitals, while the positive peak at −7.5 eV depicts the formation of a σ bond between C $2p_z$ and Cu 4*s* orbitals. Furthermore, the positive peak at −5 eV comes from σ bonds involving C $2p_z$ and Cu $3d_{z^2}$ orbitals, as well as C $2p_z$-Cu $3d_{xz}$ and C $2p_z$-Cu $3d_{yz}$ bonds without a particular symmetry. The prominent negative peak at −2 eV coincidentally includes contributions of the corresponding antibonding orbitals (C $2p_z$ with Cu $3d_{xz}$, Cu $3d_{yz}$, Cu $3d_{z^2}$ as well as to a lesser extent C $2p_z$ with Cu 4*s* and C 2*s* with Cu 4*s*). The results obtained by the orbital-resolved COHP were additionally supported by an analysis of charge difference cross-sections at the relevant C—Cu bonds (Figure S11, Supporting Information).

Finally, we note that integrating COHP curves up to the Fermi level yields the total binding energy due to the formation of covalent-like bonds (iCOHP). The inset of Figure 4d indicates iCOHPs of 0.064, 0.008, and 0.352 eV per carbon for the graphene-Cu, high separation, and low separation regimes, respectively, in MAC. This allows us to conclude that over 80% of MAC's covalent-like binding energy is due to carbon atoms from the low-separation regime. Figure 4d further shows the distance dependence of the iCOHP of individual carbon atoms for both the MAC-Cu and graphene-Cu interface (Note S2, Supporting Information). The rapid decay of the curve reinforces that the increased adhesion of MAC is primarily due to a small subset of carbon atoms positioned very close to the Cu surface, with covalent-like binding energies reaching up to 0.729 eV. This is in good agreement with the experimental observation of 13% covalent-like bonding contribution to the C 1*s* line in XPS spectra of MAC on Cu.

We conclude the discussion by comparing the covalent-like bonding energies discussed so far to the adhesion energies as calculated from first principles. The reported average covalent-like binding energies of 0.183 and 0.076 eV per carbon atom, for MAC-Cu and graphene-Cu interfaces, respectively, are in reasonable agreement with the adhesion energies of 0.097 and 0.079 eV per carbon atom. For the graphene-Cu interfaces, the results suggest that the combined effect of additional contributions toward the adhesion energy, such as van der Waals or electrostatic interactions, play only a minor role, while for MAC-Cu interfaces we expect supplementary factors, such as adhesion-induced strain

in MAC and Cu substrate, to counterbalance the strong covalent-like bonding. Notably, however, we conclude that the higher adsorption energy for MAC on Cu is primarily due to covalent-like interactions. Importantly, despite the presence of covalent-like bonding, the MAC structure remains predominantly free of sp^3 bonds and retains its continuity before and after the transfer from Cu.

3. Conclusion

In summary, we report the strong adhesion of monolayer amorphous carbon (MAC) to Cu foil surface, with an adhesion energy of 85 J m^{-2} measured by peeling tests and 13-fold enhancement when compared to graphene on Cu. KPFM analysis indicates that the van der Waals force does not significantly contribute to this interface. Instead, strong adhesion seems to originate from the formation of covalent-like Cu—C bonds, as evidenced by XPS and NEXAFS analyses. This marks the first observation of such bonding for thin carbon films on Cu. Our DFT calculations support these findings, suggesting that covalent-like bonding occurs between a subset of MAC carbon atoms and the Cu surface atoms. This study reveals that the sp^2 amorphous and corrugated structure of MAC facilitates bonding with Cu without inducing defects or requiring chemical modification, which may potentially extend to other 2D materials and substrates. The high adhesion provided by MAC, combined with its other advantageous properties–such as low temperature and direct growth capability, outstanding Cu diffusion-barrier properties,[47] high mechanical strength, and resistance to crack propagation–positions it as a promising material for applications in plasmonic devices, Cu interconnects, and solar cells.

4. Experimental Section

Synthesis of MAC: MAC films were grown by laser-assisted chemical vapour deposition. Cu foils (35 µm thickness) were first cleaned by sonication in acetone and isopropyl for 10 min, followed by 2 h of annealing in a 10 sccm H_2 flow at 0.13 Torr and 1030 °C in a quartz-tube furnace, same as the pre-annealing for graphene growth. The Cu foil was then mounted in the growth chamber and evacuated to 10^{-4} mbar. 20 sccm of CH_4 was introduced into the chamber, and the pressure was controlled at 0.03 mBar. The Cu foil was then exposed to a plasma (350 kHz pulsed d.c. generator at 5 W) and pulsed UV laser (40 mJ cm^{-2}, 50 Hz) for 10 mins. The temperature of the Cu foil was monitored by an infrared pyrometer. Stabilized temperature from laser-induced heating was controlled by the laser power. MAC was synthesized on both sides of the Cu foil. The underside film that did not experience direct exposure to the laser and plasma was used in this study.

MAC Sample Preparation: Transfer of MAC onto SiO_2/Si substrates and onto TEM grids was performed by wet transfer without a polymer support. The MAC from the top side of Cu foil was first removed by a 5-min exposure to 50 W Ar plasma. The Cu foil was etched by floating on a 1 wt.% ammonium persulfate solution. After the removal of Cu foil, the floating MAC film was scooped using a clean glass slide and rinsed twice in deionized water for 2 h. The final substrate (SiO_2/Si or TEM grid) was then used to directly scoop the MAC film out of water and dried the air. The sample was finally heated on a hot plate at 120 °C for 30 min.

Raman Spectroscopy: Raman spectra were acquired with a WITEC Alpha 300R spectrometer using either a 532 or a 633 nm laser, at room temperature. Measurements were carried out using a laser power of 1 mW and a total accumulation time of 30 s.

Adhesion Measurement: An MTS mechanical test machine was used for measuring adhesion. For the peeling test, ECA was applied to a rectangular SiO_2/Si substrate with a size of 1 × 2 cm. A MAC/Cu sample (larger than the SiO_2/Si substrate) was then placed on the ECA with MAC facing down. A glass slide was then placed on the Cu foil. The whole structure was then clamped with binder clamps to apply pressure for 2 h. After drying of ECA, the excess Cu foil over the edge of SiO_2/Si was cut off with a knife. The substrate was then glued to the bottom arm of the MTS machine by a strong double-sided tape with Cu side facing up. The first 2 mm of the Cu foil was removed manually and clamped to the top arm of the machine via a string with a length of 50 cm. The peeling force was applied vertically with respect to the SiO_2/Si substrate. The long string enabled only a small angular deviation of less than 3° during the peeling process, ensuring the applicability of the 90° peeling model.

For the shear force test, the first piece of MAC/Cu foil was placed on a glass substrate with MAC facing up. ECA was then uniformly applied to the surface of the foil. The second MAC/Cu foil was then placed on top of the first foil, creating an overlap area of 0.25 × 1 cm with MAC facing the ECA. A glass slide was then placed on the Cu foil. The whole structure was then clamped with binder clamps to apply pressure for 2 h. After drying of ECA, the whole structure was cut into a 1 cm strip with an overlap region of 0.25 × 1 cm. Two pieces of Cu foils were clamped to the top and bottom clamp of the MTS machine separately for the test.

Transmission Electron Microscopy: Dark-field TEM (DF-TEM) imaging was conducted in an FEI Tecnai F30 microscope operated at 80 kV. Images were recorded using the diffraction rings selected by the objective aperture, with an acquisition time of 120 s for each image. MAC HRTEM imaging was performed on a non-commercialized JEOL ARM60 microscope equipped with a Schottky field emission gun, a JEOL double Wien filter monochromator, double delta correctors, and a Gatan OneView camera. A slit of 2.8 µm was used for energy filtering, enabling a spatial resolution of 1.1 Å with a beam current of ≈20 pA. The microscope operated at 60 kV. STEM imaging was carried out in a JEOL 2100F microscope equipped with a Delta probe corrector, which corrected the aberration up to fifth order, resulting in a probe size of 1.0 Å. The convergent angle for illumination was ≈35 mrad, with a collection detector angle ranging from 45 to 200 mrad. A JEOL heating holder was used in all experiments to heat the sample up to 700 °C during imaging. The pair correlation function and bond angle distribution were calculated from the coordinates of the carbon atoms determined in the HRTEM and STEM images by a home-built atom-finding algorithm.

Structural Characterisation: Bruker Dimension Icon, Bruker Dimension Fastscan, and Park XE-120 atomic force microscopes were used to investigate our samples. Thickness was measured with Fastscan operated in tapping mode with Bruker FastScan A probes. Morphology was measured with Bruker Icon PeakForce tapping mode using Budget probes Multi75AlG and Park XE-120 True Non-Contact mode. Measurements of samples with varying growth time were performed with 512-pixel resolution and averaging of the profile with a 48-pixel-wide line cut. Conductive AFM was measured with PeakForce TUNA module and Pt covered tips: OSCM-PIT (15 nm tip radius) and SCT-PIT-V2 (25 nm tip radius) tips by Bruker. Additionally, measurements were reproduced using Rocky Mountain full-metal body tips with a 10 nm tip radius. For each measurement, a pure metal surface was used to check that tip conductivity remained unchanged.

The X-ray photoelectron spectroscopy (XPS) experiment was carried out using a Thermo Fisher Scientific K-Alpha instrument (USA) and a Kratos DLD Ultra XPS. The analysis chamber vacuum was $5 \bullet 10^{-10}$ Pa. The excitation source used Al Kα radiation (hv = 1486.68 eV), with a working voltage of 15 kV and a filament current of 10 mA. Signal accumulation was performed over 5–10 cycles. The pass energy was set to 50 eV with a step size of 0.05 eV. The binding energy was calibrated by using substrate peaks, such as Si 2p, Cu 2p, and Co 2p, to restore the position of C 1s lines due to the insulating nature of MAC and SiO_2/Si wafers and subsequent charging. The analysis included a survey scan Figure S6a, Supporting Information) and a detailed examination of the core level lines O 1s

(Figure S6c, Supporting Information), and Cu 2p (Figure S6d, Supporting Information).

Room temperature NEXAFS measurements and high-resolution XPS (C 1s (Figure 3g)) were performed at the GELEM dipole beamline of the BESSY-II electron storage ring operated by Helmholtz–Zentrum Berlin für Materialien und Energie as well as at FlexPES beamline of MAX IV synchrotron radiation facility. NEXAFS spectra were recorded in the total electron yield mode. The measurements were performed for the annealed (≈500 °C) samples of MAC on SiO_2/Si. All the spectra were pre- and post-edge normalized.

Kelvin Probe Force Microscopy: KPFM measurements were performed in ambient conditions using a Bruker Dimension Icon Atomic Force Microscope (AFM) with SCM-PIT-V2 cantilevers (Bruker, nominal spring constant k ~ 3 N m^{-1}) featuring a conductive Pt/Ir coating. The measurements were carried out in a dual-pass AM-KPFM mode, where the first pass scanned the topography of the sample, while the second pass recorded the surface potential using the KPFM technique in lift mode with an interleave distance of 30–50 nm.

STM and STS: Low-temperature scanning tunnelling microscopy and spectroscopy (STM/STS) measurements were performed in an Omicron low-temperature STM (≃4.2 K) under UHV conditions (≃5×10^{-11} mbar). The STM topography was measured in constant current mode using a chemically etched tungsten (W) tip. Prior to the actual measurements, the W tip was calibrated on Au (111) by voltage pulses or controlled indentations into the surface until the herringbone without artifacts and atomic resolution was achieved followed by measuring the Shockley surface states of Au (111).

Computational Methods: The initial structure of the MAC-Cu interface was set up using a Cu slab composed of 5 layers of Cu atoms, with MAC adsorbed on one side and a vacuum region greater than 25 Å to prevent spurious interactions. Each Cu layer contained 28 atoms, and the Cu-Cu distance was set to the DFT-optimized bulk value of 3.56 Å, resulting in in-plane dimensions of L_x = 17.63 Å and L_y = 16.70 Å for the orthorhombic simulation box. The amorphous carbon layer was generated using a quench-from-the-melt method starting from a pristine graphene plane with 112 atoms under periodic boundary conditions.[45] The melting (>9000 K) and subsequent cooling (<300 K) of the carbon network were simulated within the canonical (NVT) ensemble with friction coefficient τ = 1 ps and Adaptive Intermolecular Reactive Empirical Bond Order (AIREBO) force field coefficients using the classical molecular dynamics code Large-scale Atomic/Molecular Massively Parallel simulator (LAMMPS).[46–50] The amorphicity of the carbon monolayer could be effectively controlled by adjusting the cooling rate, where a rate of τ_c = 0.71 K/fs perfectly reproduced the ring distribution observed in the experimental structure (see Figure S7, Supporting Information). Finally, the MAC structure was stretched to fit the Cu simulation box (strain <5% along every axis) and placed at a distance of 3.0 Å from the Cu.

A complementing study of the Gr-Cu interface was done similarly, the initial setup consisting of a slab of 7 Cu atom layers having graphene adsorbed on one side and a vacuum region >25 Å. The in-plane dimensions of the Gr-Cu system were set to L_x = 2.52 Å and L_y = 8.35 Å, corresponding to 2 Cu atoms per layer with bulk-optimized Cu-Cu distance. A 4 × 1 supercell of graphene was stretched (strain < 5%) to fit the simulation box and placed again at a distance of 3 Å from the Cu substrate.

DFT calculations were subsequently performed using a plane-wave basis set and the Projector Augmented Wave (PAW) formalism[51,52] as implemented in the Vienna Ab Initio Simulation Package (VASP).[53–56] A kinetic energy cutoff of 520 eV was set, and the Perdew–Burke–Ernzerhof (PBE) exchange-correlation functional was used in conjunction with the Grimme D3 van der Waals correction to accurately account for weak interactions at the interface.[56,57] Ground-state properties and atomic positions for both the MAC-Cu and Gr-Cu systems were retrieved after relaxing the initial structures (detailed in the above section) with a force tolerance of 0.05 eV $Å^{-1}$, keeping the simulation box fixed and only allowing the ions to move. The k-point grids were 1 × 1 × 1 for the MAC-Cu interface and 40 × 13 × 1 for the Gr-Cu interface models.

Supporting Information

Supporting Information is available from the Wiley Online Library or from the author.

Acknowledgements

The authors are grateful to Professor Yuri Gogotsi for fruitful discussions. B.Ö. acknowledges support by the National Research Foundation, Prime Minister's Office, Singapore, under its Competitive Research Programme (CRP award number NRF-CRP22-2019-008), National Research Foundation Investigatorship (NRFI award no. NRF-NRFI2018-08), and Medium-Sized Centre Programme (CA2DM), by EDB Singapore, under its Space Technology Development Programme (S22-19013-STDP), and by the Ministry of Education of Singapore, under its MOE-ACRF-Tier 2 (Award no. MOE-T2EP50220-0017), and Research Centre of Excellence award to the Institute for Functional Intelligent Materials (I-FIM, Project No. EDUNC-33-18-279-V12). H.Z. and O.V.Y. acknowledge support by the Swiss National Science Foundation (grant No. 204254). B.W. acknowledges the support of the National Research Foundation (NRF) Singapore, under the Competitive Research Program "Towards On-Chip Topological Quantum Devices" (NRF-CRP21-2018-0001), with further support from the Singapore Ministry of Education (MOE) Academic Research Fund Tier 3 grant (MOE-MOET32023-0003) "Quantum Geometric Advantage". M. K. acknowledges support from the Ministry of Education, Singapore, under its Academic Research Fund Tier 2 (MOE-T2EP50122-0012) and Air Force Office of Scientific Research and the Office of Naval Research Global under award number FA8655-21-1-7026. M.B. acknowledges support by the Ministry of Education of Singapore, via Academic Research Fund Tier 2 (MOE-T2EP50122-0016). N.K., Y.S. and K.S. acknowledge support by the JST CREST (JPMJCR20B1). The authors acknowledge MAX IV Laboratory for experimental time on the FlexPES beamline under Proposal No. 20231842. Research conducted at MAX IV, a Swedish national user facility, is supported by the Swedish Research Council under Contract No. 2018–07152, the Swedish Governmental Agency for Innovation Systems under Contract No. 2018–04969, and Formas under Contract No. 2019-0249. We thank the Helmholtz-Zentrum Berlin für Materialien und Energie for the allocation of synchrotron radiation beamtime at GELEM Dipole. We are grateful to Alexei Preobrajenski and Alexander Generalov, staff members at the FlexPES, for their strong interest and support of this research. Computations were performed at the Swiss National Supercomputing Centre (CSCS) under project No. s1299 and the facilities of the Scientific IT and Application Support Centre of EPFL.

Conflict of Interest

The authors declare no conflict of interest.

Author Contributions

H.Z. and A.K.G. contributed equally to this work. B.Ö. initiated the work. A.K.G. coordinated the experiments. K.V.I. and H.Z. performed adhesion energy experiments. R.S.K., Z.J.T. and B.W. performed STM imaging. Y.H. and M.B. performed cross-section TEM imaging. A.M., A.F. and D.V.V. performed XPS and NEXAFS experiments. H.Z., R.Y. and O.V.Y. performed DFT calculations. S.G., M.K. and K.S.N. performed KPFM experiments. U.K., L.S., A.K.G., H.Z., A.S., K.I., A.S., A.A., C.C.T., and C.M.O. synthesized and characterized samples. J.L., K.S. performed HRTEM imaging. H.Z., A.K.G., C.T.T. and B.O. wrote the manuscript. C.T.T. and B.O. supervised the project. All authors discussed the results and contributed to the manuscript.

Data Availability Statement

The data that support the findings of this study are available from the corresponding author upon reasonable request.

Keywords

2D material, amorphous carbon, copper, interfacial adhesion

Received: December 6, 2024
Revised: April 29, 2025
Published online: May 29, 2025

[1] J. R. Davis, in *Copper and Copper Alloys*, ASM International, Materials Park, OH, USA **2001**.
[2] V. G. Kravets, R. Jalil, Y.-J. Kim, D. Ansell, D. E. Aznakayeva, B. Thackray, L. Britnell, B. D. Belle, F. Withers, I. P. Radko, Z. Han, S. I. Bozhevolnyi, K. S. Novoselov, A. K. Geim, A. N. Grigorenko, *Sci. Rep.* **2014**, *4*, 5517.
[3] R. K. Singh Raman, P. C. Banerjee, D. E. Lobo, H. Gullapalli, M. Sumandasa, A. Kumar, L. Choudhary, R. Tkacz, P. M. Ajayan, M. Majumder, *Carbon* **2012**, *50*, 4040.
[4] C. Mattevi, H. Kim, M. Chhowalla, *J. Mater. Chem.* **2011**, *21*, 3324.
[5] A. K. Geim, K. S. Novoselov, *Nat. Mater.* **2007**, *6*, 183.
[6] J. Hong, S. Lee, S. Lee, H. Han, C. Mahata, H.-W. Yeon, B. Koo, S.-I. Kim, T. Nam, K. Byun, B.-W. Min, Y.-W. Kim, H. Kim, Y.-C. Joo, T. Lee, *Nanoscale* **2014**, *6*, 7503.
[7] K. P. Loh, S. W. Tong, J. Wu, *J. Am. Chem. Soc.* **2016**, *138*, 1095.
[8] L. Camilli, F. Yu, A. Cassidy, L. Hornekær, P. Bøggild, *2D Mater.* **2019**, *6*, 022002.
[9] R. Jiang, X. Zhou, Z. Liu, *Mater. Sci. Eng. A* **2017**, *679*, 323.
[10] K. Chu, F. Wang, X. Wang, Y. Li, Z. Geng, D. Huang, H. Zhang, *Mater. Des.* **2018**, *144*, 290.
[11] Y.-Y. Sin, C.-C. Huang, C.-N. Lin, J.-K. Chih, Y.-L. Hsieh, I.-Y. Tsao, J. Li, C.-Y. Su, *Carbon* **2020**, *169*, 248.
[12] K. Chu, J. Wang, Y. Liu, Z. Geng, *Carbon* **2018**, *140*, 112.
[13] C.-T. Toh, H. Zhang, J. Lin, A. S. Mayorov, Y.-P. Wang, C. M. Orofeo, D. B. Ferry, H. Andersen, N. Kakenov, Z. Guo, I. H. Abidi, H. Sims, K. Suenaga, S. T. Pantelides, B. Özyilmaz, *Nature* **2020**, *577*, 199.
[14] B. Shin, B. Ni, C.-T. Toh, D. Steinbach, Z. Yang, L. M. Sassi, Q. Ai, K. Niu, J. Lin, K. Suenaga, Y. Han, M. J. Buehler, B. Özyilmaz, J. Lou, *Matter* **2025**, *8*, 102000.
[15] E. Griffin, L. Mogg, G.-P. Hao, G. Kalon, C. Bacaksiz, G. Lopez-Polin, T. Y. Zhou, V. Guarochico, J. Cai, C. Neumann, A. Winter, M. Mohn, J. H. Lee, J. Lin, U. Kaiser, I. V. Grigorieva, K. Suenaga, B. Özyilmaz, H.-M. Cheng, W. Ren, A. Turchanin, F. M. Peeters, A. K. Geim, M. Lozada-Hidalgo, *ACS Nano* **2020**, *14*, 7280.
[16] E. Andideh, T. Scherban, B. Sun, J. Blaine, C. Block, B. Jin, in Proc. IEEE 2001 Int. Interconnect Technology Conf., Burlingame, CA, USA, June **2001**, 257.
[17] C. J. Shearer, A. D. Slattery, A. J. Stapleton, J. G. Shapter, C. T. Gibson, *Nanotechnology* **2016**, *27*, 125704.
[18] A. Eckmann, A. Felten, I. Verzhbitskiy, R. Davey, C. Casiraghi, *Phys. Rev. B* **2013**, *88*, 035426.
[19] M. M. Lucchese, F. Stavale, E. H. M. Ferreira, C. Vilani, M. V. O. Moutinho, R. B. Capaz, C. A. Achete, A. Jorio, *Carbon* **2010**, *48*, 1592.
[20] Y. Han, K. C. Lai, A. Lii-Rosales, M. C. Tringides, J. W. Evans, P. A. Thiel, *Surf. Sci.* **2019**, *685*, 48.
[21] D. Akinwande, C. J. Brennan, J. S. Bunch, P. Egberts, J. R. Felts, H. Gao, R. Huang, J.-S. Kim, T. Li, Y. Li, K. M. Liechti, N. Lu, H. S. Park, E. J. Reed, P. Wang, B. I. Yakobson, T. Zhang, Y.-W. Zhang, Y. Zhou, Y. Zhu, *Extreme Mech. Lett.* **2017**, *13*, 42.
[22] P. h. Martiny, F. Lani, A. J. Kinloch, T. Pardoen, *Int. J. Adhes. Adhes.* **2008**, *28*, 222.
[23] T. Yoon, W. C. Shin, T. Y. Kim, J. H. Mun, T.-S. Kim, B. J. Cho, *Nano Lett.* **2012**, *12*, 1448.
[24] S. R. Na, J. W. Suk, L. Tao, D. Akinwande, R. S. Ruoff, R. Huang, K. M. Liechti, *ACS Nano* **2015**, *9*, 1325.
[25] M. D. Bartlett, S. W. Case, A. J. Kinloch, D. A. Dillard, *Prog. Mater. Sci.* **2023**, *137*, 101086.
[26] Q. Zhao, N. Hong, D. Chen, W. Li, *J. Dyn. Syst. Meas. Control* **2022**, *144*, 071004.
[27] N. Hong, Q. Zhao, D. Chen, K. M. Liechti, W. Li, *Carbon* **2023**, *201*, 712.
[28] H. W. Coover, D. W. Dreifus, J. T. O'Connor, in *Handbook of Adhesives* (Ed.: I. Skeist), Springer US, Boston, MA, USA **1990**, pp. 463–477.
[29] K. Donnelly, D. P. Dowling, M. L. McConnell, M. Mooney, *Thin Solid Films* **2001**, *394*, 101.
[30] P.-P. Cortet, M.-J. Dalbe, C. Guerra, C. Cohen, M. Ciccotti, S. Santucci, L. Vanel, *Phys. Rev. E* **2013**, *87*, 022601.
[31] E. Ringoot, T. Roch, J.-F. Molinari, T. J. Massart, T. Cohen, *J. Mech. Phys. Solids* **2021**, *155*, 104528.
[32] S. Flege, R. Hatada, W. Ensinger, K. Baba, *Surf. Coat. Technol.* **2014**, *256*, 37.
[33] W. R. L. Lambrecht, *Phys. B Condens. Matter* **1993**, *185*, 512.
[34] Z. Liu, S. Zheng, Z. Lu, J. Pu, G. Zhang, *Carbon* **2018**, *127*, 548.
[35] J. Wintterlin, M.-L. Bocquet, *Surf. Sci.* **2009**, *603*, 1841.
[36] H. Lu, X. Huang, D. Li, *J. Appl. Phys.* **2014**, *116*, 173506.
[37] P. A. Khomyakov, G. Giovannetti, P. C. Rusu, G. Brocks, J. van den Brink, P. J. Kelly, *Phys. Rev. B* **2009**, *79*, 195425.
[38] R. C. Setiawan, M. Wu, D. Y. Li, *Langmuir* **2022**, *38*, 1672.
[39] W.-H. Lin, T.-H. Chen, J.-K. Chang, J.-I. Taur, Y.-Y. Lo, W.-L. Lee, C.-S. Chang, W.-B. Su, C.-I. Wu, *ACS Nano* **2014**, *8*, 1784.
[40] G. A. Haas, R. E. Thomas, *J. Appl. Phys.* **1977**, *48*, 86.
[41] W. Zhang, A. Nefedov, M. Naboka, L. Cao, C. Wöll, *Phys. Chem. Chem. Phys.* **2012**, *14*, 10125.
[42] A. Matruglio, S. Nappini, D. Naumenko, E. Magnano, F. Bondino, M. Lazzarino, S. Dal Zilio, *Carbon* **2016**, *103*, 305.
[43] C. Ehlert, W. E. S. Unger, P. Saalfrank, *Phys. Chem. Chem. Phys.* **2014**, *16*, 14083.
[44] A. B. Preobrajenski, M. L. Ng, A. S. Vinogradov, N. Mårtensson, *Phys. Rev. B* **2008**, *78*, 073401.
[45] R. Ravinder, R. Kumar, M. Agarwal, N. M. A. Krishnan, *Sci. Rep.* **2019**, *9*, 4517.
[46] R. Dronskowski, P. E. Bloechl, *J. Phys. Chem.* **1993**, *97*, 8617.
[47] Y.-H. Kang, S. Lee, Y. Choi, W. K. Seong, K. H. Han, J. H. Kim, H.-M. Kim, S. Hong, S. H. Lee, R. S. Ruoff, K.-B. Kim, S. O. Kim, *Adv. Mater.* **2022**, *34*, 2110454.
[48] S. Nosé, *J. Chem. Phys.* **1984**, *81*, 511.
[49] W. G. Hoover, *Phys. Rev. A* **1985**, *31*, 1695.
[50] A. P. Thompson, H. M. Aktulga, R. Berger, D. S. Bolintineanu, W. M. Brown, P. S. Crozier, P. J. in 't Veld, A. Kohlmeyer, S. G. Moore, T. D. Nguyen, R. Shan, M. J. Stevens, J. Tranchida, C. Trott, S. J. Plimpton, *Comput. Phys. Commun.* **2022**, *271*, 108171.
[51] G. Kresse, D. Joubert, *Phys. Rev. B* **1999**, *59*, 1758.
[52] G. Kresse, J. Hafner, *J. Phys. Condens. Matter* **1994**, *6*, 8245.
[53] G. Kresse, J. Hafner, *Phys. Rev. B* **1993**, *47*, 558.
[54] G. Kresse, J. Hafner, *Phys. Rev. B* **1994**, *49*, 14251.
[55] G. Kresse, J. Furthmüller, *Comput. Mater. Sci.* **1996**, *6*, 15.
[56] G. Kresse, J. Furthmüller, *Phys. Rev. B* **1996**, *54*, 11169.
[57] J. P. Perdew, K. Burke, M. Ernzerhof, *Phys. Rev. Lett.* **1996**, *77*, 3865.